8092 J. Phys. Chem. A **2003,** *107,* 8092−8105

Energy-Level Diagrams and Their Contribution to Fifth-Order Raman and Second-Order Infrared Responses: Distinction between Relaxation Models by Two-Dimensional Spectroscopy†

Ko Okumura*

Department of Physics, Graduate School of Humanities and Sciences, Ochanomizu, University, 2-1-1, Otsuka, Bunkyo-ku, Tokyo 112-8610, Japan, and Physique de la Matière Condensée, Collège de France, 11 place Marcelin-Berthelot, 75231 Paris Cedex 05, France

Yoshitaka Tanimura

Theoretical Studies, Institute for Molecular Science, Okazaki, Aichi 444-8585, Japan

Received: October 31, 2002; In Final Form: February 13, 2003

We develop a Feynman rule for energy-level diagrams emphasizing their connections to the double-sided Feynman diagrams and physical processes in the Liouville space. Thereby, we completely identify such diagrams and processes contributing to the 2D response function in the Brownian oscillator model. We classify such diagrams or processes in quartets and numerically present signals separately from each quartet of diagrams or Liouville-space processes. We find that the signal from each quartet is distinctly different from the others; we can identify each peak in the frequency domain with a certain quartet. This provides the basis for analyzing and assigning actual 2D peaks and suggests the possibility of Liouville-space path-selective spectroscopy. As an application, we demonstrate an example in which two familiar homogeneous models of relaxation are distinguished by the existence or nonexistence of certain peaks on the 2D map; the appearance or disappearance of certain peaks is sensitive to the choice of coupling models. We also point out some confusion in the literature with regard to the inclusion of relaxation effects.

I. Introduction

The use of ultrashort laser pulses to probe the properties of molecules has been propelled by rapid advances in laser measurement techniques.[1] Recently, 2D vibrational spectroscopy has been actively studied, where the spectral properties of multibody correlation functions of polarizability (2D Raman spectroscopy)[2−19] or dipole moments (2D infrared spectroscopy)[20−23] are measured. The 2D technique provides information about the inter- and intramolecular interactions that cause energy relaxations.[24−28]

Theoretically, optical responses of molecular vibrational motions have been studied mainly by either an oscillator model[29] or an energy-level model.[30] The oscillator model utilizes molecular coordinates to describe molecular motions. This description is physically intuitive since optical observables (dipole moments or Raman polarizabilities) are also described by molecular coordinates; the effects of relaxation, which are caused by interactions of the coordinate with some other degrees of freedom, are rather easy to include. As long as the potential is harmonic or nearly harmonic, signals can be calculated analytically.[2,6,31−35]

On the contrary, the energy-level model employs the energy eigenfunctions of a molecular motion but is physically equivalent to the oscillator model. Accordingly, laser interactions are described by transitions between the energy levels; the optical processes, including the time ordering of laser pulses, are conveniently described by diagrams such as Albrecht diagrams[36] or double-sided Feynman diagrams.[1] Although the inclusion of relaxation processes from physical insight is less intuitive and is restricted to some special cases, this model has the advantage of identifying peak positions of the optical signal in the frequency domain.[37−40] The anharmonicity of potential and nonlinear mode−mode coupling is also easily taken into account. Phase-matching conditions, which chose a specific Liouville path contribution by the configuration of laser beams,[1] are also easy to take into account. In the oscillator model or molecular dynamics simulations, the phase-matching condition can be used only after calculating entire response functions.[41] The rate of increase in the number of diagrams, however, with the increase in laser interactions is more severe in the energy-level model than in the oscillator model; this becomes a serious practical problem for multidimensional spectroscopy, where many laser interactions are included.[6]

In this paper, we try to bridge the two complementary models by transferring some results obtained in the oscillator model to the energy-level language. Although we lose simplicity (e.g., the small number of diagrams), we gain insight into the optical processes; we can assign each peak to a certain set of optical or Liouville-space processes. The resulting energy-level Feynman rule for the oscillator system allows the inclusion of relaxation in an ad hoc way. As an application, we compare two system with different damping constants. This example reveals that the existence of certain peaks in the 2D spectroscopic map sensitively depends on the relaxation model.

II. Interaction of Energy-Level Diagrams

We consider a molecular vibrational motion described by a single molecular coordinate Q. In the energy-level representa-

---

[†] Part of the special issue “A. C. Albrecht Memorial Issue”.

[*] Corresponding author. E-mail: okumura@phys.ocha.ac.jp.

10.1021/jp027360o CCC: $25.00 © 2003 American Chemical Society
Published on Web 05/20/2003

tion, the Hamiltonian is expressed as

$$H_0 = \hbar\Omega\left(a^\dagger a + \frac{1}{2}\right) \tag{1}$$

where a and $a^\dagger$ are the creation and annihilation operators, respectively, and

$$Q = \sqrt{\frac{\hbar}{2M\Omega}}\,(a + a^\dagger) \tag{2}$$

for the system with mass M. The energy levels of this harmonic system are given by $E_n = \hbar\Omega_n$ with $\Omega_n = (n + 1/2)\Omega$ for which we introduce the frequency difference $\Omega_{mn} = \Omega_m - \Omega_n$. If the system interacts with the laser field $E(t)$, then it is governed by the full Hamiltonian

$$H(t) = \begin{cases} H_0 + \mu E(t) & \text{(IR)} \\ H_0 + \alpha E(t)^2 & \text{(Raman)} \end{cases} \tag{3}$$

where μ is the dipole for infrared (IR) and α is the polarizability for Raman spectroscopy. Both operators can be expanded as

$$x = x_0 + x_1 Q + \frac{1}{2!}x_2 Q^2 + \frac{1}{3!}x_3 Q^3 + \cdots \tag{4}$$

We consider the response function

$$R^{(2)}(T_1, T_2) = \theta(t_3 - t_2)\,\theta(t_2 - t_1)\left\langle\left[\left[x(t_3), \frac{\mathrm{i}}{\hbar}x(t_2)\right], \frac{\mathrm{i}}{\hbar}x(t_1)\right]\right\rangle \tag{5}$$

which is pertinent to 2D second-order IR (for nonisotropic media) or 2D fifth-order Raman spectroscopy, where $x(t)$ is the Heisenberg operator of x for the noninteracting Hamiltonian H_0 and $\langle O\rangle \equiv \mathrm{Tr}[\rho_0 O]$ with $\rho_0 = \mathrm{e}^{-\beta H_0}/\mathrm{Tr}[\mathrm{e}^{-\beta H_0}]$. (When we include the effect of dissipation at the level of the Hamiltonian, H_0 includes the bath Hamiltonian and the system−bath interaction.) The operator x stands for μ (IR) or α (Raman). The generalization to the combined IR and Raman cases such as $\langle[[\mu(t_3), \mu(t_2)], \alpha(t_1)]\rangle$[28, 42−44] will also be treated below.

$R^{(2)}(T_1, T_2)$ for the harmonic system can be expanded in terms of Q by eq 4. The leading order is given as

$$R^{(2)}(T_1, T_2) = \left(\frac{i}{\hbar}\right)^2 \frac{x_1^2 x_2}{2}(R_1 + R_2 + R_3) \tag{6}$$

where

$$R_1 = \langle[[Q^2(T_1 + T_2), Q(T_1)], Q(0)]\rangle \tag{7}$$

$$R_2 = \langle[[Q(T_1 + T_2), Q^2(T_1)], Q(0)]\rangle \tag{8}$$

$$R_3 = \langle[[Q(T_1 + T_2), Q(T_1)], Q^2(0)]\rangle \tag{9}$$

with

$$\begin{cases} t_3 - t_2 = T_2 \\ t_2 - t_1 = T_1 \end{cases} \tag{10}$$

A. Raman Spectroscopy. For the moment, we concentrate on the Raman case (i.e., $\langle[[\alpha(t_3), \alpha(t_2)], \alpha(t_1)]\rangle$). Some of the processes in eq 6 are represented by the energy-level (Albrecht-like) diagrams in Figure 1. The differences from the original Albrecht diagram are mentioned at the end of this section. Before explaining the diagrams, let us review the rudiments of possible transitions by operators Q and Q^2; Q can cause a one-quantum excitation or de-excitation whereas Q^2 can result in a two-quantum excitation or de-excitation in addition to a zero-quantum transition. For example, from $|0\rangle \rightarrow Q^2|0\rangle \sim [(a^\dagger)^2 + aa^\dagger]|0\rangle$, we see that by the action of the operator Q^2 the ground ket state $|0\rangle$ can be converted into $|0\rangle$ (zero-quantum transition) or $|2\rangle$ (two-quantum excitation). In the same way, $\langle 2|$ can be brought into $\langle 0|$ (two-quantum de-excitation) or $\langle 2|$ (zero-quantum transition).

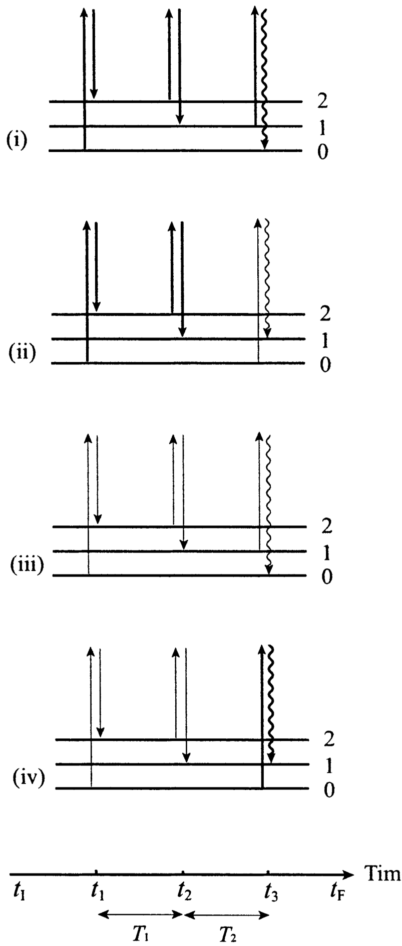

Figure 1. Energy-level diagrams of $R^{(2)}(T_1, T_2)$ for Raman processes.

In the diagrams, time runs from the left to the right. Each pair of arrows stands for a Raman excitation. The pair with a wavy arrow signifies the Raman induction decay (*last* interaction). The first interaction occurs at t_1; the second, at t_2; and the last, at t_3.

The full description of a quantum state at a certain time requires both the bra state $\langle n|$ and the ket state $|m\rangle$; at any time the state is fully specified by the Liouville state $|m\rangle\langle n|$. In the diagrams, the excitation or de-excitation of the *bra* state is expressed by a pair of *thin* arrows whereas that of the *ket* state, by *thick* ones. For example, the first interaction at t_1 of (i) and (ii) is a two-quantum excitation of the ket state whereas that of (iii) and (iv) is of the bra state.

In the Liouville space, the diagram (i) is interpreted as follows. The system is initially in the ground (Liouville) state $|0\rangle\langle 0|$. The first interaction causes a two-quantum excitation of the ket state, $|0\rangle\langle 0| \rightarrow |2\rangle\langle 0|$ at t_1. The second interaction causes a one-quantum de-excitation, $|2\rangle\langle 0| \rightarrow |1\rangle\langle 0|$ at t_2. The last shows a one-quantum de-excitation, $|1\rangle\langle 0| \rightarrow |0\rangle\langle 0|$ at t_3. As a whole, we denote this as

$$|0\rangle\langle 0| \xrightarrow{t_1} |2\rangle\langle 0| \xrightarrow{t_2} |1\rangle\langle 0| \xrightarrow{t_3} |0\rangle\langle 0| \tag{11}$$

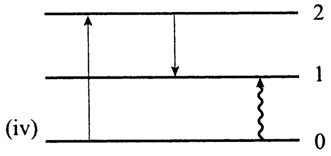

Figure 2. Energy-level diagram of $R^{(2)}(T_1, T_2)$ for IR processes.

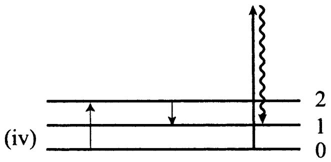

Figure 3. Energy-level diagrams of $R^{(2)}(T_1, T_2)$ for IR−Raman processes, $\langle[[\mu(t_3), \mu(t_2)], \alpha(t_1)]\rangle$.

The diagrams (ii)−(iv) are interpreted as follows:

$$|0\rangle\langle 0| \xrightarrow{t_1} |2\rangle\langle 0| \xrightarrow{t_2} |1\rangle\langle 0| \xrightarrow{t_3} |1\rangle\langle 1| \tag{12}$$

$$|0\rangle\langle 0| \xrightarrow{t_1} |0\rangle\langle 2| \xrightarrow{t_2} |0\rangle\langle 1| \xrightarrow{t_3} |0\rangle\langle 0| \tag{13}$$

$$|0\rangle\langle 0| \xrightarrow{t_1} |0\rangle\langle 2| \xrightarrow{t_2} |0\rangle\langle 1| \xrightarrow{t_3} |1\rangle\langle 1| \tag{14}$$

Note here that a pair of *thin* arrows always correspond to the excitation or de-excitation of the *bra* state.

We define the population state by $|n\rangle\langle n|$ and the coherence state by $|n\rangle\langle m|$ ($n \neq m$). We notice that, after the last interaction, in all of the above four diagrams, the system is always in a population state ($|0\rangle\langle 0|$ or $|1\rangle\langle 1|$). In summary, *a diagram does not vanish only when the final state is a population state* (Theorem 1). This corresponds to the trace operation in the definition of the response function.

In this paper, we simplify the original Albrecht diagrams[36] for comparison with the Liouville paths. The main differences are the following: (1) we always use the same horizontal lines regardless of ket or bra states, which is not the case in the original Albrecht diagrams and (2) time always runs from left to right in our representation whereas the directions for the bra and ket states are the opposite in the original version. Our representation is somewhat simpler in that a single diagram in ours sometimes corresponds to several diagrams in the original version.

B. IR and IR−Raman Spectroscopy. IR processes appearing in the IR response function, $\langle[[\mu(t_3), \mu(t_2)], \mu(t_1)]\rangle$, corresponding to Figure 1(iv) is described in Figure 2; each quantum transition is represented not by a pair of arrows but one arrow. Note that Raman and IR processes can be equivalent theoretically at this level of description, although even orders of IR processes, such as second-order IR signals, vanish except in anisotopic media, such as adsorbed molecules on metallic surfaces.[45] This situation can be overcome by mixing the IR and Raman processes.[42] By using narrow-band lasers (two IR excitation pulses followed by one probe pulse that creates a Raman signal), Zhao and Wright demonstrated such an experiment.[28,44]

As in IR−Raman spectroscopy, we consider the response function $\langle[[\alpha(t_3), \mu(t_2)], \mu(t_1)]\rangle$, for example. A diagram corresponding to Figure 1(iv) is shown in Figure 3; Raman and IR transitions are represented by a pair of arrows and by one arrow, respectively. Diagrams corresponding to the other IR−Raman response function such as $\langle[[\mu(t_3), \mu(t_2)], \alpha(t_1)]\rangle$ can be described in a similar manner.

III. Energy-Level Diagram and Double-Sided Diagram

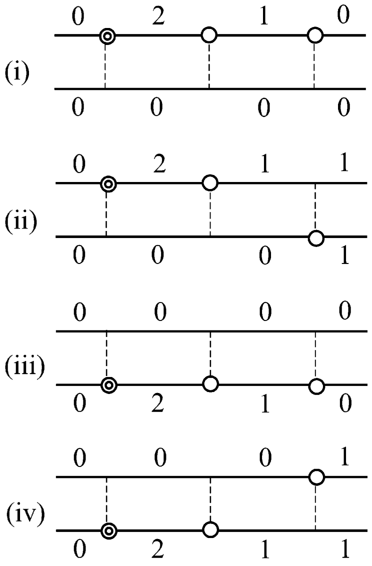

Figure 4. Double-sided Feynman diagrams of $R^{(2)}(T_1, T_2)$.

We can represent processes in the Liouville space in a different way by the double-sided Feynman diagrams. The diagrams in Figure 4 are the translations of the diagrams in Figures 1, 2, or 3. In the double-sided diagrams, time runs from the left to right (as in the energy-level diagram). However, there are always two horizontal lines—the upper and lower lines. The former represents the ket state whereas the latter, the bra state. The single circle stands for a one-quantum transition whereas the double circle stands for a two-quantum transition. The quantum number of the bra and ket states is denoted explicitly in the diagram.

It is noted that there are some differences in diagrammatic notation among articles. For example, in some literature, the quantum transition is not represented by circles but by arrows. In another one, diagrams are rotated by 90° so that the time runs from the bottom to the top.

In general, as seen below (section VI. A), *the double-sided diagram is convenient for enumerating all possible diagrams whereas the energy-level diagram is convenient for understanding the physical process.*

IV. Feynman Rules for the Diagrams

We have introduced several ways to represent optical processes as in Figures 1−4. It is emphasized here that the interpretation in terms of the Liouville-space state $|m\rangle\langle n|$ is unique except for what x_k implies. Accordingly, we can develop a universal rule to write down analytical expressions from diagrams via the interpretations (such as eqs 11−14) in the Liouville space; the derivation is a straightforward exercise in elementary quantum mechanics and will be discussed elsewhere. It can be summarized in the following way. We associate with each interaction (originating from the interaction $Q^k/k!$) at a certain time or each propagation for a certain period one of the factors shown in Table 1 or 2: By multiplying all of the factors

TABLE 1: Factors for Interaction

interaction ($n \geq 0$)	factor
$|m\rangle \rightarrow |m+n\rangle$	$(i/\hbar)x_k\langle m+n|\, Q^k|\, m\rangle/k!$
$|m\rangle \rightarrow |m-n\rangle$	$(i/\hbar)x_k\langle m-n|\, Q^k|m\rangle/k!$
$\langle m| \rightarrow \langle m+n|$	$(-i/\hbar)x_k\langle m|\, Q^k|m+n\rangle/k!$
$\langle m| \rightarrow \langle m-n|$	$(-i/\hbar)x_k\langle m|\, Q^k|\, m-n\rangle/k!$
remark	omit $\pm\, i/\hbar$ for the last interaction

TABLE 2: Factors for Propagation

propagation ($t \geq 0$)	factor
$|m\rangle\langle n|$ for t	$e^{-i\xi_{mn}t - \Gamma_{mn}t}$

and inserting another factor of 1/2 to avoid double counting (see Theorem 2 below), we obtain an analytical expression of the corresponding diagram (*Feynman rule*). Here, we have introduced ζ_{mn} and Γ_{mn} (≥ 0) to describe relaxation; the difference in frequency, which was modified due to the relaxation, is defined by $\zeta_{mn} = (m - n)\zeta$ whereas the relaxation constant Γ_{mn} for the state $|m\rangle\langle n|$ possesses the symmetric property $\Gamma_{nm} = \Gamma_{mn}$, which is a necessary condition for a consistent theory (see the comment just below eq 21). Without dissipation, $\zeta_{mn} \rightarrow \Omega_{mn} = (m - n)\Omega$ and $\Gamma_{mn} \rightarrow 0$. In the Brownian oscillator model with the damping constant γ, the corrected frequency ζ is given by $\zeta = \sqrt{\Omega^2 - (\gamma/2)^2}$.[46,47] The expression for Γ_{mn} in this model shall be discussed below.

By definition, *the propagation period* implies the time *between two interactions*. This excludes the periods from t_I to t_1 and from t_3 to t_F in the diagrams in Figures 1−4 (or, say, in eqs 11−14) because there is no interaction at t_I or t_F; we associate the unity for these special periods.

Let us apply our rule without relaxation ($\Gamma_{mn} = 0$, $\zeta_{mn} = \Omega_{mn}$) to a diagram or a Liouville-space path. As the first example, we consider diagram (i) (of Figure 1 or 4). We have only two separate propagation periods by definition. In the first period from t_1 to t_2, the system is in state $|2\rangle\langle 0|$, and thus we have the factor $e^{-i\Omega_{20}(t_2 - t_1)}$ whereas for the last period from t_2 to t_3 the system is in state $|1\rangle\langle 0|$ and we have the factor $e^{-i\Omega_{10}(t_3 - t_2)}$; in total, we have the propagation factor $e^{-i\Omega_{20}T_1}\cdot e^{-i\Omega_{10}T_2}$, where we have used relation 10. In addition, as the result of the three interactions, we have other factors:

$$\frac{i}{\hbar}x_2\frac{\langle 2|Q^2|0\rangle}{2}\cdot\frac{i}{\hbar}x_1\langle 1|Q|2\rangle\cdot x_1\langle 0|Q|1\rangle = \left(\frac{i}{\hbar}\frac{\hbar}{2M\Omega}x_1\right)^2 x_2$$

(Note here the relations eq 2 as well as $a|n\rangle = \sqrt{n}|n-1\rangle$ and $a^\dagger|n\rangle = \sqrt{n+1}|n+1\rangle$). In summary, the process in eq 11 or diagram (i) is given (with the extra factor of 1/2 associated with the double counting) by

$$\text{(i)} = \left(\frac{i}{\hbar}\right)^2\frac{x_1^2x_2}{2}\left(\frac{\hbar}{2M\Omega}\right)^2 e^{-i2\Omega T_1}\cdot\ e^{-i\Omega T_2} \tag{15}$$

The process in eq 12 or diagram (ii) (of Figure 1 or 4) is different from (i) only after t_3. Although the last interaction at t_3 is that for the bra state (expressed by the thin arrows and different form (i)), the factors for this last interaction is the same as that of (i) by the above Feynman rule; there is no sign differences between the bra and ket states especially for the last interaction. In summary we have

$$\text{(ii)} = \text{(i)} \tag{16}$$

In general, we have the following theorem, which is related to the double counting: *The diagrams that are different only by the side of the last interaction (bra or ket side) have the same contribution* (Theorem 2).

The process in eq 13 or in diagram (iii) can be estimated in a similar manner by the above Feynman rule:

$$\text{(iii)} = \left(-\frac{i}{\hbar}\right)^2\frac{x_1^2x_2}{2}\left(\frac{\hbar}{2M\Omega}\right)^2 e^{i2\Omega T_1}\cdot\ e^{i\Omega T_2} \tag{17}$$

Note here the minus sign in front of i/ħ because of the interactions on the bra state (thin arrows). From t_1 to t_2, the system is in states $|0\rangle\langle 2|$ and $|2\rangle\langle 0|$ in (iii) and (i), respectively; these two states are the complex conjugates of each other. From t_2 to t_3, the state of (iii), $|0\rangle\langle 1|$, is again in the complex-conjugate state of (i), $|1\rangle\langle 0|$. Accordingly, (iii) given above is the complex conjugate of (i) (i.e., (iii) = (i)*). Diagrammatically, in (iii) of Figure 1, all of the thick arrows in (i) are replaced by thin arrows. In general, *the complex-conjugate diagram is obtained by interchanging all of the thick and thin arrows* (Theorem 3). In the double-sided Feynman diagrams, instead, *the complex-conjugate diagram is obtained by interchanging the circles on the upper and lower lines* (Theorem 3′).

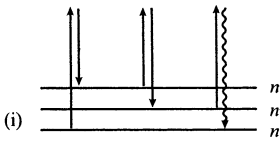

Figure 5. General process corresponding to Figure 1(i)

Diagram (iv) is the complex-conjugate diagram of (ii) because the thin and thick arrows are interchanged (i.e., (iv) = (ii)*). We can also verify the relation (iii) = (iv) from the above Feynman rule by reconfirming Theorem 2.

V. Temperature Effect and Initial State

In the above discussion, we have assumed that the system is initially in the ground state, $|0\rangle\langle 0|$, which is usually justified for high-frequency vibrational modes at room temperature. For high temperatures or low-frequency modes, however, excited states $|n\rangle\langle n|$ are initially populated according to the Boltzmann factor. In general, we have to estimate all of the possible processes assuming that the system is initially in the population state $|n\rangle\langle n|$ using the above-mentioned rule and then summing with respect to n with the Boltzmann factor $e^{-\beta E_n}/\sum_n e^{-\beta E_n}$ (where E_n is the eigenvalue of H_0 in the case without dissipation); this completes our Feynman rule.

Even if we take into account the contribution from the general initial state $|n\rangle\langle n|$, however, in the (fully corrected) Ohmic Brownian oscillator model, we still obtain the same result as above as shown in the literature. This is the reflection of the relation

$$\langle n|X|n\rangle = \langle 0|X|0\rangle \tag{18}$$

where X is some special combination of operators. (This could be directly checked by laborious calculations using our Feynman rule.) The fact that $R^{(2)}(T_1, T_2)$ treated in this paper is independent of the temperature, and thus we can obtain a finite temperature result even if we assume that the system is initially in the ground state, is by no means trivial but is established by other calculation methods.[6] This implies, for example, that the dependence on n of the analytical expression corresponding to Figure 5 cancels out with some other diagram. For damping models other than the (fully corrected) Ohmic Brownian oscillator model, our results presented below might be interpreted as a high-frequency approximation (i.e., $\hbar\Omega \gg kT$.)

VI. Liouville-Space Quartet

The four diagrams (i)−(iv) in Figures 1 and 4 are a special set in the sense that we can obtain the other three starting from one of the quartets.

In the energy-level diagram, we obtain the second by changing the last interaction by using one of the following rules (depending on the last interaction of the starting diagram): (1) the (last) ket excitation to a bra de-excitation, (2) the ket de-excitation to a bra excitation, (3) the bra excitation to a ket de-excitation, or (4) the bra de-excitation to a ket excitation. The remaining two diagrams are the complex-conjugate diagrams of the previous two diagrams. (The conjugates are obtained by interchanging the thin and thick arrows.)

In the double-sided diagram, the second diagram is obtained by lowering or raising the last circle. The remaining two are obtained by interchanging the lower and upper lines with circles.

As seen before, the corresponding analytical expressions of (i)−(iv) have the relations (i) = (ii), (iii) = (iv), and (i) = (iii)* . The sum of the quartet is always real:

$$\text{(i)} + \text{(ii)} + \text{(iii)} + \text{(iv)} = 4\mathrm{Re}[\text{(i)}] = 4\mathrm{Re}[(n)] \tag{19}$$

where n = i, ii, iii, or iv. Taking the real part of eq 15, we have an expression for the quartet,

$$V_{\mathrm{I}} = -\frac{x_1^2 x_2}{2(M\Omega)^2}\cos(2\Omega T_1 + \Omega T_2) \tag{20}$$

In terms of the interpretation in the Liouville space in eqs 11−14, all of the processes possess a common property: the two-quantum coherence ($|2\rangle\langle 0|$ or $|0\rangle\langle 2|$) is realized for T_1 whereas the one-quantum coherence ($|1\rangle\langle 0|$ or $|0\rangle\langle 1|$) is realized for T_2; we denote this as

$$|2\rangle\langle 0| \rightarrow |1\rangle\langle 0| \quad \text{and} \quad |0\rangle\langle 2| \rightarrow |0\rangle\langle 1| \tag{21}$$

This is reflected by the factor $\cos(2\Omega T_1 + \Omega T_2)$ in eq 20.

We notice that in the case with damping if Γ_{mn} (and ζ_{mn}) were not symmetric then V_{I} could not be real; the symmetric property of Γ_{mn} is required for the response function to be real.

A. Quartet Representations: All Possible Quartets for *$R^{(2)}(T_1, T_2)$*. We show six quartets R(1)−R(6) in Figure 6 in the double-sided representation. The square brackets imply the quartet; only one of the quartets is explicitly written in the brackets. For example, R(1) of Figure 6 collectively stands for (i)−(iv) of Figure 4.

In Figure 6, on the right side, 10 quartets in the energy-level representation are given; some quartets in double-sided representation correspond to not one but two quartets in the energy-level representation. For example, R(1) contains contributions I and I′ whereas R(3) contains only A2.

Six quartets R(1)−R(6) in Figure 6 exhaust all possible contributions to the right-hand side of eq 6; there are 3 ways to put in the double-quantum transition (double circle), and there 2^3 ways to position the three (including one double circle) circles on the upper or lower line, which leads to $3\cdot 2^3$ double-sided Feynman diagrams in total. These $3\cdot 8$ diagrams can be divided into 6 quartets that have been shown. We understand here that *the double-sided diagram is convenient for enumerating all possible diagrams.*

B. Estimation of Quartets. The analytical expression of quartet II is given via our Feynman rule:

$$\mathrm{II} = 4\mathrm{Re}\left[-\left(\frac{i}{\hbar}\right)^2\left(\frac{\hbar}{2M\zeta}\right)^2 \cdot \frac{x_1^2 x_2}{2} \cdot \mathrm{e}^{-i2\zeta T_1 - \Gamma_{20}T_1} \cdot \mathrm{e}^{-i\zeta T_2 - \Gamma_{21}T_2}\right] \tag{22}$$

where the analytical expression in the square brackets has been derived from the diagram explicitly drawn in the brackets in Figure 6 (in the presence of dissipation). For example, the propagators $\mathrm{e}^{-i2\zeta T_1 - \Gamma_{20}T_1}$ and $\mathrm{e}^{-i\zeta T_2 - \Gamma_{21}T_2}$ come from the propagation of $|2\rangle\langle 0|$ and $|2\rangle\langle 1|$, respectively.

In this way, we obtain the expression

$$R^{(2)}(T_1, T_2) = \mathrm{I} + \mathrm{II} + \mathrm{A} + \mathrm{B} + \mathrm{C} + \mathrm{D1} + \mathrm{D2} \tag{23}$$

where these labels (I, II, A, ...) correspond to those in Figure 6 and their analytical expressions are given as follows:

$$\mathrm{I} = -\frac{x_1^2 x_2}{2(M\zeta)^2}\mathrm{e}^{-\Gamma_{20}T_1 - \Gamma_{10}T_2}\cos(2\zeta T_1 + \zeta T_2) \tag{24}$$

$$\mathrm{II} = \frac{x_1^2 x_2}{2(M\zeta)^2}\mathrm{e}^{-\Gamma_{20}T_1 - \Gamma_{21}T_2}\cos(2\zeta T_1 + \zeta T_2) \tag{25}$$

$$\mathrm{A} = -\frac{x_1^2 x_2}{2(M\zeta)^2}\mathrm{e}^{-\Gamma_{10}T_1 - \Gamma_{10}T_2}\cos(\zeta T_1 + \zeta T_2) \tag{26}$$

$$\mathrm{B} = \frac{x_1^2 x_2}{2(M\zeta)^2}\mathrm{e}^{-\Gamma_{10}T_1 - \Gamma_{12}T_2}\cos(\zeta T_1 - \zeta T_2) \tag{27}$$

$$\mathrm{C} = -\frac{x_1^2 x_2}{2(M\zeta)^2}\mathrm{e}^{-\Gamma_{10}T_1 - \Gamma_{20}T_2}\cos(\zeta T_1 + 2\zeta T_2) \tag{28}$$

$$\mathrm{D1} = -\frac{1}{4}\frac{x_1^2 x_2}{(M\zeta)^2}\mathrm{e}^{-\Gamma_{10}T_1 - \Gamma_{00}T_2}\cos(\zeta T_1) \tag{29}$$

$$\mathrm{D2} = \frac{3}{4}\frac{x_1^2 x_2}{(M\zeta)^2}\mathrm{e}^{-\Gamma_{10}T_1 - \Gamma_{11}T_2}\cos(\zeta T_1) \tag{30}$$

As for the derivation of this, we remark: (1) Quartets I′ and II′ cancel out because

$$\mathrm{I}' = -\frac{1}{4}\frac{x_1^2 x_2}{(M\zeta)^2}\mathrm{e}^{-\Gamma_{00}T_1 - \Gamma_{10}T_2}\cos(\zeta T_2)$$

and

$$\mathrm{II}' = \frac{1}{4}\frac{x_1^2 x_2}{(M\zeta)^2}\mathrm{e}^{-\Gamma_{00}T_1 - \Gamma_{01}T_2}\cos(\zeta T_2)$$

(The numerical factor 1/4 can be understood from the first two-quantum transition associated with $\langle 0|Q^2|0\rangle \propto \langle 0|aa^\dagger|0\rangle = 1$.) (2) The sum A2 + A1 reduces to A. (The numerical factor for A2 (or A1) can be estimated by noting the second two-quantum transition $\langle 1|Q^2|1\rangle \propto \langle 1|aa^\dagger + a^\dagger a|1\rangle = 3$ (or $\langle 0|Q^2|0\rangle \propto \langle 0|aa^\dagger|0\rangle = 1$)).

It is worthwhile to observe the relationships between analytical expressions and the symbolic interpretations of the remaining quartets:

$$\mathrm{A}: \ |1\rangle\langle 0| \rightarrow |1\rangle\langle 0| \quad \text{and} \quad |0\rangle\langle 1| \rightarrow |0\rangle\langle 1| \tag{31}$$

$$\mathrm{B}: \ |1\rangle\langle 0| \rightarrow |1\rangle\langle 2| \quad \text{and} \quad |0\rangle\langle 1| \rightarrow |2\rangle\langle 1| \tag{32}$$

$$\mathrm{C}: \ |1\rangle\langle 0| \rightarrow |2\rangle\langle 0| \quad \text{and} \quad |0\rangle\langle 1| \rightarrow |0\rangle\langle 2| \tag{33}$$

$$\mathrm{D1}: \ |1\rangle\langle 0| \rightarrow |0\rangle\langle 0| \quad \text{and} \quad |0\rangle\langle 1| \rightarrow |0\rangle\langle 0| \tag{34}$$

$$\mathrm{D2}: \ |1\rangle\langle 0| \rightarrow |1\rangle\langle 1| \quad \text{and} \quad |0\rangle\langle 1| \rightarrow |1\rangle\langle 1| \tag{35}$$

That is, we can associate the state $|n\rangle\langle m|$ with ζ_{nm} and Γ_{mn}.

We note that, in principle, if we fully included the temperature effect by our Feynman rule with tracking all of the possible processes, then we could obtain the result given in Appendix B of ref 37.

VII. Damping Models

We can confirm that the well-known result for the Ohmic Brownian oscillator (BO) model (Ohmic implies that the system-

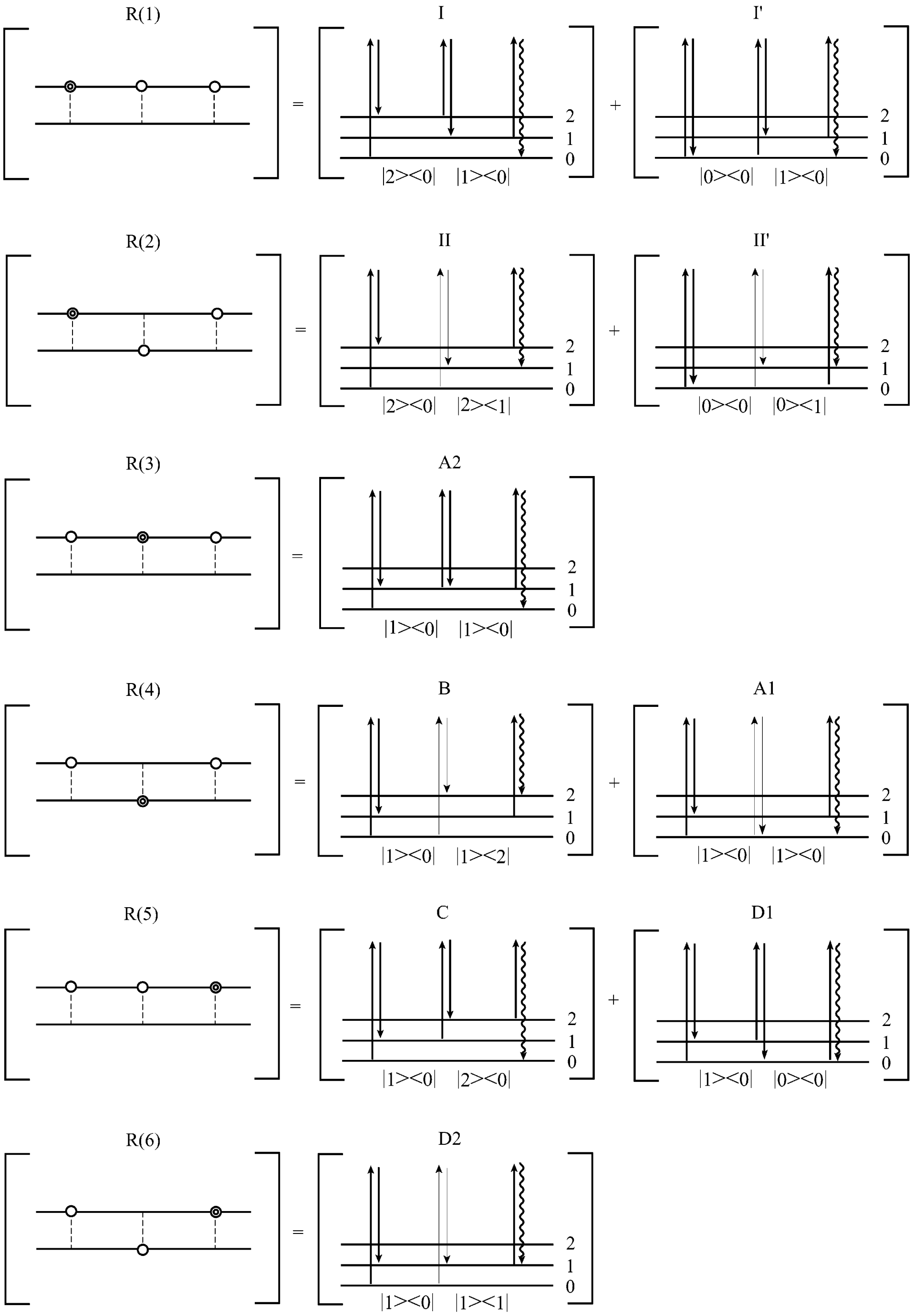

Figure 6. All possible quartets for $R^{(2)}(T_1, T_2)$. The square brackets imply that four diagrams are collectively represented. For example, the first diagram in the energy-level diagram for R(1) corresponds not only to (i) of Figure 1 (which is explicitly written in the brackets) but also to the other three diagrams (ii)−(iv) of Figure 1.

bath coupling is in the bilinear form) is reproduced from eq 23 by setting

$$\Gamma_{nm} = \begin{cases} \gamma & \text{for } |n\rangle\langle n| \\ |n-m|\gamma/2 & \text{for } |n\rangle\langle m|\ (n \neq m) \end{cases} \tag{36}$$

where $|m|$ represents the absolute value of m. Actually, in the Brownian result, I + II should be zero, which is true if $\Gamma_{21} = \Gamma_{10}$, while D1 + D2 should be −2D1, which is true if $\Gamma_{11} = \Gamma_{00}$; Γ_{mn} in eq 36 satisfies these requirements.

The cancellation of I and II is one of the features of the Brownian result. Another feature is that the state $|0\rangle\langle 0|$ decays with the relaxation constant γ, which is the same as that for $|1\rangle\langle 1|$. These characteristics have provoked some controversy, as mentioned below.

The relaxation constant for the same Ohmic model within the lower-level approximation (i.e., at the level of Fermi's golden rule with a somewhat ad hoc approximation (see below)) is given by refs 37 and 48

$$\Gamma_{mn} = \frac{n+m}{2}\gamma \tag{37}$$

which is also simple but incompatible with the above two requirements ($\Gamma_{21} = \Gamma_{10}$ and $\Gamma_{11} = \Gamma_{00}$). With this relaxation constant, I and II survive, for example. (In addition, there is no frequency shift ($\zeta_{mn} \rightarrow \Omega_{mn}$) in this finite-order approximation.)

The frequency shift and appearance of the absolute value ($|n - m|$), which is *nonanalytic* in the off-diagonal relaxation constant, in eq 36, may correspond to the summation of an infinite number of diagrams. In the well-known result of the Ohmic BO model, *the bilinear coupling between the system-bath is fully taken into account*; this is the exact prediction from a simple reasonable model, and we are concerned with the relaxation of *fully dressed states* in the exact result of the BO model. On the contrary, the relaxation constant in eq 37 is the result of the same model but with the second-order (in coupling strength) approximation. Nonetheless, in some contexts, the second-order result has been favored whereas the full-order result has been questioned.[37,49]

As we show below, we can distinguish the above two models (36 or 37) by a 2D experiment by checking for the existence or absence of certain peaks. In other words, whether the coherence (off-diagonal) relaxation constant that depends only on the quantum number difference (where $\Gamma_{m+n,m} = \Gamma_{n,0}$) and the level-independent population relaxation are appropriate (as the first-order picture) or not might be checked experimentally.

Note that if the system has some sort of anharmonicity such as the anharmonicity of potential[29] or the nonlinear system-bath coupling[50] then the relaxation constants do not follow $\Gamma_{21} = \Gamma_{10}$ and so forth, even when we take into account higher-order system−bath interactions. Then the number of Liouville paths involved in the optical processes increase dramatically, especially when the system−bath interaction is very strong. Also, if the laser−molecular interaction is much shorter than the time duration of the system−bath interactions, then one has to regard the relaxation rate as a function of time (i.e., $\Gamma_{nm}(t)$). In such case, the equation-of-motion approach is more appropriate than the diagrammatic approaches, although it requires computationally expensive calculations.[50−55]

We comment on the confusion in the literature with regard to the Redfield theory, one example of which is eq 37. The Redfield theory without the rotational wave approximation (RWA) is equivalent to the Fokker−Planck equation.[51−55] The time-evolution operator in the Liouville space from state $|k, l\rangle\rangle \equiv |k\rangle\langle l|$ to $\langle\langle i, j| \equiv \langle i|\cdots|j\rangle$ is then expressed as $\langle\langle i, j|e^{-i(\hat{H}^{\times}-\hat{\Gamma})t}|k, l\rangle\rangle$, where $\hat{H}^{\times}$ is the quantum Liouvillian and $\hat{\Gamma}$ is the damping operator (Redfield operator). In an energy-level representation, $|k, l\rangle\rangle$ is the eigenfunction of the Hamiltonian but not the eigenfunction of $\hat{\Gamma}$, which makes it difficult to evaluate this propagator. However, one sometimes reads the damping constant directly from the Redfield tensor elements Γ_{ijkl} and incorporates them in the propagator as $\langle\langle i, j|e^{-i(\hat{H}^{\times}-\Gamma_{ijkl})t}|k, l\rangle\rangle$, which cannot be justified from the coordinate representation model.[37,48] Accordingly, this ad hoc methodology possesses a flaw in the sense that the theory thus obtained does not converge to analytical perturbative results such as those obtained by the Brownian oscillator model. It is possible to evaluate effective tensor element $\Gamma_{ijkl}^{(\mathrm{eff})}$ by solving the equation of motion such as the Fokker−Planck equation with linear and nonlinear system−bath interactions,[50−55] but the calculated results are quite different from the Redfield tensor elements.[50]

VIII. Multimode System

Extension to the multimode system, whose characteristic modes are represented by $\{Q_s\}$, $\{M_s\}$, and $\{\gamma_s\}$, is straightforward.[22,33,39,56] We expand the dipole or polarizability operator as

$$x = x_0 + \sum_s x_1^{(s)} Q^{(s)} + \frac{1}{2!}\sum_{s,s'} x_2^{(ss')} Q^{(s)} Q^{(s')} + \cdots \tag{38}$$

and we denote the Liouville state by

$$|\{n_s\}\rangle\langle\{n'\}| = (|n_1\rangle\langle n_1'|)_1 \cdots (|n_s\rangle\langle n'_s|)_s \cdots \tag{39}$$

where $\{n_s\} = (n_1, n_2, \cdots)$ is the quantum number of the corresponding mode. Hereafter, we use the notation in which $|n_s, n_{s'}\rangle\langle m_s, m_{s'}|$ stands for the state where the modes s and s' are in the states $|n_s\rangle\langle m_s|$ and $|n_s'\rangle\langle m_s'|$, respectively. For example, $|0, 1\rangle\langle 2, 3|$ means that the first and second modes are in the ground and first excited ket states while they are in the second and third excited bra states, respectively.

The factor (in the Feynman rule) for the transition is well explained by example. The transition

$$|0, 0\rangle\langle 0, 0| \rightarrow |2, 1\rangle\langle 0, 0| \tag{40}$$

caused by the operator $(Q^{(1)})^2 Q^{(2)}$ is associated with the factor

$$\frac{1}{3!}\cdot\frac{i}{\hbar}(x_3^{(112)} + x_3^{(121)} + x_3^{(211)})\langle 2, 1|(Q^{(1)})^2 Q^{(2)}|0, 0\rangle = \frac{1}{2!}\cdot\frac{i}{\hbar}x_3^{(112)}\sqrt{2}\frac{\hbar}{M_1\Omega_1}\sqrt{\frac{\hbar}{M_2\Omega_2}}$$

whereas the transition (again caused by $(Q^{(1)})^2 Q^{(2)}$)

$$|0, 0\rangle\langle 0, 0| \rightarrow |0, 0\rangle\langle 2, 1| \tag{41}$$

is associated with the same factor with the minus sign. If the above transition occurs at the last time, however, we have to omit the factor $i/\hbar$ as in the single-mode case.

Note here that a transition of the type

$$|0, 0\rangle\langle 0, 0| \rightarrow |1, 0\rangle\langle 1, 0| \tag{42}$$

cannot occur at once, but

$$|0, 0\rangle\langle 0, 0| \rightarrow |1, 1\rangle\langle 0, 0| \tag{43}$$

can occur; bra and ket excitation can never occur simultaneously, that is, the simultaneous multitransition can occur exclusively for the ket state or for the bra state.

The time propagation factor of each mode in the state $(|n\rangle\langle m|)_s$ during a (positive) time duration t is given by $e^{-i(n-m)\Omega_s t}$ for the harmonic system without dissipation.

In the multimode case, the diagram explicitly written in the square brackets labeled D2 in Figure 6 represents either a single-mode process

$$\begin{cases} |1\rangle\langle 0| & \rightarrow & |1\rangle\langle 1| & (\text{mode } s) \\ - & \rightarrow & - & (\text{mode } s') \end{cases} \tag{44}$$

where − implies no time propagation, or a two-mode process

$$\begin{cases} |1\rangle\langle 0| & \rightarrow & |1\rangle\langle 0| & (\text{mode } s) \\ - & \rightarrow & |0\rangle\langle 1| & (\text{mode } s') \end{cases} \tag{45}$$

which is explicitly shown in the square brackets labeled D2 in Figure 7. In other words, in the multimode case, quartet D2 in Figure 6 represents the quartets displayed in Figure 8.

By using the above rules in the multimode case, we see that the propagator of the process in eq 45 is given by $e^{-i\Omega_s T_1}\cdot e^{-i(\Omega_s - \Omega_{s'})T_2}$ because $|1, 0\rangle\langle 0, 0|$ propagates for T_1 and $|1, 0\rangle\langle 0, 1|$ propagates for T_2. The remaining interaction factors are

$$\frac{1}{2!}\cdot\frac{i}{\hbar}x_1^{(s)}\langle 1, 0|Q^{(s)}|0, 0\rangle\cdot\left(-\frac{i}{\hbar}\right)x_1^{(s')}\langle 0, 0|Q^{(s')}|0, 1\rangle \cdot(x_2^{(ss')} + x_2^{(s's)})\langle 0, 1|Q^{(s)}Q^{(s')}|1, 0\rangle$$

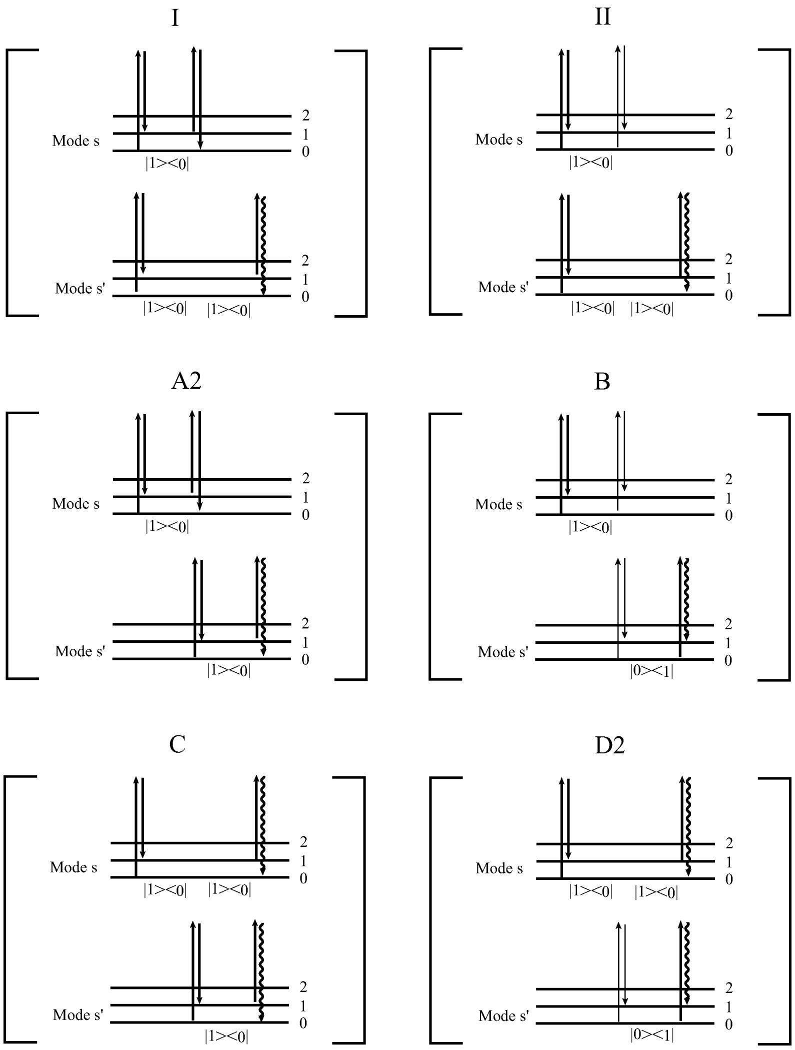

Figure 7. Two-mode processes. There are no counterparts to I′, II′, A1, and D1.

(and the factor 1/2 is included to avoid double counting). Taking into account the other elements of the quartets, we obtain the total contribution D2 of Figure 6 in the multimode case in the form

$$\mathrm{D2} = 4\sum_{s,s'}\mathrm{Re}\left[-\frac{1}{2}c_{ss'}\left(\frac{i}{\hbar}\right)^2 x_1^{(s)}x_1^{(s')}x_2^{(ss')} \times \frac{\hbar}{2M_s\Omega_s}\frac{\hbar}{2M_{s'}\Omega_{s'}}\,\mathrm{e}^{-i\Omega_s\mathrm{T}_1}\,\mathrm{e}^{-\mathrm{i}(\Omega_s-\Omega_{s'})T_2}\right] \quad (46)$$

where $c_{ss'}$ is 1 and 3/2 for $s \neq s'$ and $s = s'$, respectively. Comparing this with diagrams, we learn that we should associate $|n_s, n_{s'}\rangle\langle m_s, m_{s'}|$ with $\Omega^{(s)}_{n_s m_s} + \Omega^{(s')}_{n_{s'} m_{s'}}$. These four quartets correspond to four diagrams in Figure 8 (in the dissipationless case).

In this way (now taking into account the effect of dissipation), we have

$$R^{(2)}(T_1, T_2) = \sum_{s=1,2}(\mathrm{I}_s + \mathrm{II}_s + \mathrm{B}_s + \mathrm{C}_s + \mathrm{D1}_s + \mathrm{D2}_s) + \sum_{s,s'}\mathrm{A2}_{ss'} + \sum_{s,s'}{}'(B_{ss'} + C_{ss'} + D_{ss'}) \quad (47)$$

where the prime in the expression, $\sum_{s,s'}{}'$ implies that the terms with $s = s'$ are excluded in the sum. Here, each term is given by

$$\mathrm{I}_s = -f_{ss}\,\mathrm{e}^{-\Gamma^{(s)}_{20}T_1 - \Gamma^{(s)}_{10}T_2}\cos(2\zeta_s T_1 + \zeta_s T_2) \quad (48)$$

$$\mathrm{II}_s = f_{ss}\,\mathrm{e}^{-\Gamma^{(s)}_{20}T_1 - \Gamma^{(s)}_{21}T_2}\cos(2\zeta_s T_1 + \zeta_s T_2) \quad (49)$$

$$\mathrm{A2}_{ss'} = -f_{ss'}\,\mathrm{e}^{-\Gamma^{(s)}_{10}T_1 - \Gamma^{(s')}_{10}T_2}\cos(\zeta_s T_1 + \zeta_{s'} T_2) \quad (50)$$

$$\mathrm{B}_s = f_{ss}\,\mathrm{e}^{-\Gamma^{(s)}_{10}T_1 - \Gamma^{(s)}_{12}T_2}\cos(\zeta_s T_1 - \zeta_s T_2) \quad (51)$$

$$\mathrm{B}_{ss'} = f_{ss'}\,\mathrm{e}^{-\Gamma^{(s)}_{10}T_1 - \Gamma^{(s')}_{01}T_2}\cos(\zeta_s T_1 - \zeta_{s'} T_2) \quad (52)$$

$$\mathrm{C}_s = -f_{ss}\,\mathrm{e}^{-\Gamma^{(s)}_{10}T_1 - \Gamma^{(s)}_{20}T_2}\cos(\zeta_s T_1 + 2\zeta_s T_2) \quad (53)$$

$$\mathrm{C}_{ss'} = -f_{ss'}\,\mathrm{e}^{-\Gamma^{(s)}_{10}T_1 - (\Gamma^{(s)}_{10} + \Gamma^{(s')}_{10})T_2} \quad (54)$$

$$\times\cos(\zeta_s T_1 + (\zeta_s + \zeta_{s'})T_2) \quad (55)$$

$$\mathrm{D1}_s = -\frac{1}{2}f_{ss}\,\mathrm{e}^{-\Gamma^{(s)}_{10}T_1 - \Gamma^{(s)}_{00}T_2}\cos(\zeta_s T_1) \quad (56)$$

$$\mathrm{D2}_s = \frac{3}{2}f_{ss}\,\mathrm{e}^{-\Gamma^{(s)}_{10}T_1 - \Gamma^{(s)}_{11}T_2}\cos(\zeta_s T_1) \quad (57)$$

$$\mathrm{D2}_{ss'} = f_{ss'}\,\mathrm{e}^{-\Gamma^{(s)}_{10}T_1 - (\Gamma^{(s)}_{10} + \Gamma^{(s')}_{10})T_2} \quad (58)$$

$$\times\cos(\zeta_s T_1 + (\zeta_s - \zeta_{s'})T_2) \quad (59)$$

with

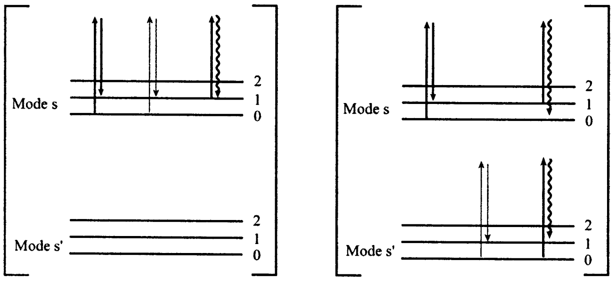

Figure 8. Quartets represented by quartet D of Figure 6.

$$f_{ss'} = \frac{x_1^{(s)} x_1^{(s')} x_2^{(ss')}}{2M_s\zeta_s M_{s'}\zeta_{s'}} \tag{60}$$

We observe the following: (1) I $_{ss'}$ and II $_{ss'}$ always cancel out whereas I$_s$ and II$_s$ cancel out only if

$$\Gamma_{10}^{(s)} = \Gamma_{21}^{(s)} \tag{61}$$

(2) The sum (A1 + A2)$_s$ is given by letting $s' \rightarrow s$ in A2$_{ss'}$. (3) When we use

$$\Gamma_{nn}{}^{(s)} = \begin{cases} \gamma_s/2 & \text{for } |n_s\rangle\,\langle n_s| \\ |n_s - m_s|\gamma_s/2 & \text{for } |n_s\rangle\,\langle m_s|\ (n_s \neq m_s) \end{cases} \tag{62}$$

the above expression reduces to the result of the fully corrected Brownian oscillator model. If we employ the model with the relaxation constant

$$\Gamma_{mn}^{(s)} = \frac{n+m}{2}\gamma_s \tag{63}$$

then this leads to a different result; one of the feature is the survival of the single-mode terms I$_s$ and II$_s$.

IX. Feynman Rule in Frequency Domain

In the frequency domain, we study the quantity

$$\int_0^\infty d\omega_1 \int_0^\infty d\omega_2\, e^{i\omega_1 T_1 + i\omega_2 T_2} R^{(2)}(T_1, T_2) \tag{64}$$

The frequency domain expression is obtained by using the above propagators in the frequency domain (or, instead, directly by the Fourier transformation of eq 47). The general propagating factor in the multimode case, $e^{-\Gamma T_1 - i\Omega T_1} \cdot e^{-\Gamma' T_2 - i\Omega' T_2}$, is, in the frequency domain, replaced by

$$\frac{i}{\omega_1 - \Omega + i\Gamma} \cdot \frac{i}{\omega_2 - \Omega' + i\Gamma'} \tag{65}$$

The expression of eq 47 in the frequency domain is given in the Appendix.

X. Two-Dimensional Signal from Each Liouville-Space Quartet

In this section, we present 2D signals from each Liouville-space quartet separately in the fully corrected Brownian oscillator model. In the frequency domain, since the signal is a complex number, we show the absolute value of the signal. In the time domain, the signal is real, which is directly shown.

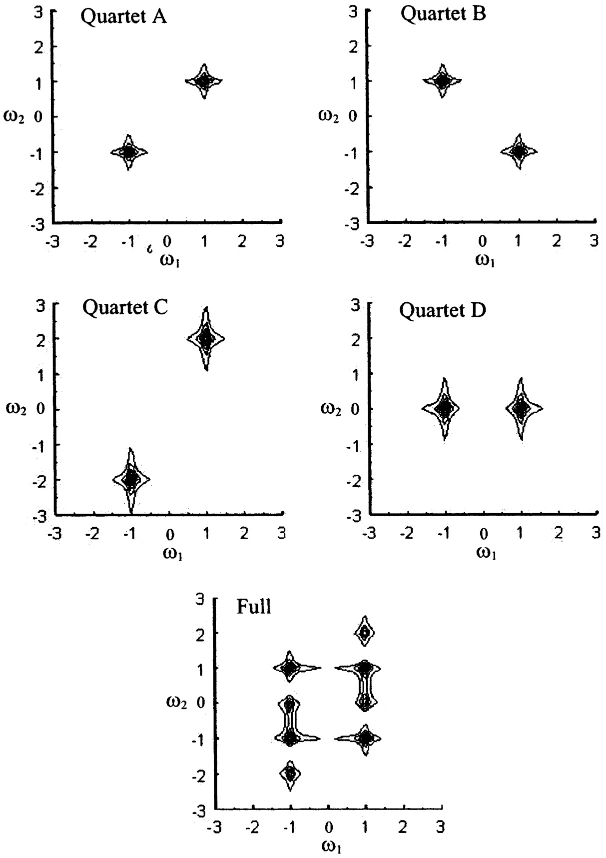

Figure 9. Contour plot of the signal from the system with a single mode with weak damping. The upper four plots correspond to the separate contributions from each Liouville-space quartet. The bottom plot is the sum of them (i.e., the total signal).

A. Frequency Domain. A1. Single Mode (Weak Damping). Figure 9 shows signals from the system with a single mode ($\Omega = 1$, $\gamma = 0.1$, in arbitrary units). Signals from each Liouville space quartet are shown separately. We can interpret each peak in the following way. The process represented by $|n\rangle\,\langle m| \rightarrow |n'\rangle\,\langle m'|$ implies that the system is in state $|n\rangle\,\langle m|$ for T_1 and $|n'\rangle\,\langle m'|$ for T_2. Then, we assign Ω_{nm} and Γ_{nm} for T_1 and $\Omega_{n'm'}$ and $\Gamma_{n'm'}$ for T_2. This can be symbolically written as

$$|n\rangle\,\langle m| \rightarrow |n'\rangle\,\langle m'| \Rightarrow \begin{cases} (\Omega_{nm}, \Omega_{n'm'}) \\ (\Gamma_{nm}, \Gamma_{n'm'}) \end{cases} \tag{66}$$

Actually, the process $|n\rangle\,\langle m| \rightarrow |n'\rangle\,\langle m'|$ corresponds to the peak at $(\omega_1, \omega_2) = (\Omega_{nm}, \Omega_{n'm'})$ with the widths in the ω_1 and ω_2 axes given by Γ_{nm} and $\Gamma_{n'm'}$, respectively. This results from the expression in eq 65 and can be confirmed numerically as we see below.

We note here that we need not consider the contributions from quartets I and II because they cancel each other in the fully corrected Brownian oscillator model.

Quartets A = A1 + A2. This is symbolized by $|1\rangle\,\langle 0| \rightarrow |1\rangle\,\langle 0|$ and its complex conjugate $|0\rangle\,\langle 1| \rightarrow |0\rangle\,\langle 1|$. The former process can be symbolically written as

$$|1\rangle\,\langle 0| \rightarrow |1\rangle\,\langle 0| \Rightarrow \begin{cases} (\Omega_{10}, \Omega_{10}) \\ (\Gamma_{10}, \Gamma_{10}) \end{cases} \Rightarrow \begin{cases} (\Omega, \Omega) \\ (\gamma/2, \gamma/2) \end{cases} \tag{67}$$

This suggests a diagonal peak $(\omega_1, \omega_2) = (\Omega, \Omega)$ whose widths in the ω_1 and ω_2 directions are $\gamma/2$; this peak shows a symmetric pattern with respect to the two axes, which can be seen in the contour plot in Figure 9. With the complex conjugate process $|0\rangle\,\langle 1| \rightarrow |0\rangle\,\langle 1|$, we associate

$$|1\rangle\,\langle 0| \rightarrow |1\rangle\,\langle 0| \Rightarrow \begin{cases} (\Omega_{01}, \Omega_{01}) \\ (\Gamma_{01}, \Gamma_{01}) \end{cases} \Rightarrow \begin{cases} -(\Omega, \Omega) \\ (\gamma/2, \gamma/2) \end{cases} \tag{68}$$

Namely, quartet pair A corresponds to two symmetric diagonal peaks at $(\omega_1, \omega_2) = \pm(\Omega, \Omega.)$ (See the top left plot of Figure 9.)

Quartet B. Symbolically, the association is as follows:

$$|1\rangle\langle 0| \to |1\rangle\langle 2| \Rightarrow \begin{cases}(\Omega_{10}, \Omega_{12})\\(\Gamma_{10}, \Gamma_{12})\end{cases} \Rightarrow \begin{cases}(\Omega, -\Omega)\\(\gamma/2, \gamma/2)\end{cases} \tag{69}$$

Its complex conjugate is

$$|1\rangle\langle 0| \to |2\rangle\langle 1| \Rightarrow \begin{cases}(\Omega_{01}, \Omega_{21})\\(\Gamma_{01}, \Gamma_{21})\end{cases} \Rightarrow \begin{cases}(-\Omega, \Omega)\\(\gamma/2, \gamma/2)\end{cases} \tag{70}$$

Namely, we have two symmetric diagonal peaks at $(\omega_1,\omega_2) = \pm(\Omega, -\Omega)$. (See the top right plot of Figure 9.)

Quartet C. In a similar way, from the association

$$|1\rangle\langle 0| \to |2\rangle\langle 0| \Rightarrow \begin{cases}(\Omega_{10}, \Omega_{20})\\(\Gamma_{10}, \Gamma_{20})\end{cases} \Rightarrow \begin{cases}(\Omega, -2\Omega)\\(\gamma/2, \gamma)\end{cases} \tag{71}$$

and its conjugate, we should have two significant overtone peaks at $(\omega_1, \omega_2) = \pm(\Omega, 2\Omega)$ whose width in the ω_1 direction is one-half of that in the ω_2 direction; the peak is elongated in the second axis, as can be seen in the contour plot in Figure 9. (See the middle left plot of Figure 9.)

Quartet D = D1 + D2. From the associations

$$\text{D1: } |1\rangle\langle 0| \to |0\rangle\langle 0| \Rightarrow \begin{cases}(\Omega_{10}, \Omega_{00})\\(\Gamma_{10}, \Gamma_{00})\end{cases} \Rightarrow \begin{cases}(\Omega, 0)\\(\gamma/2, \gamma)\end{cases} \tag{72}$$

$$\text{D2: } |1\rangle\langle 0| \to |1\rangle\langle 1| \Rightarrow \begin{cases}(\Omega_{10}, \Omega_{11})\\(\Gamma_{10}, \Gamma_{11})\end{cases} \Rightarrow \begin{cases}(\Omega, 0)\\(\gamma/2, \gamma)\end{cases} \tag{73}$$

and their complex conjugates, we should have two significant elongated axial peaks at $(\omega_1, \omega_2) = (\pm\Omega, 0)$. (See the middle right plot of Figure 9.)

The total signal displayed at the bottom of Figure 9 shows eight significant peaks; now that we know from which Liouville-space path each peak originates, *we can assign each peak with distinct Liouville-space paths* by the data in Table 3.

TABLE 3: Peak Positions for Quartets

quartet	peak positions in (ω_1, ω_2) plane
A	$(\Omega, \Omega), (-\Omega, -\Omega)$
B	$(\Omega, -\Omega), (-\Omega, \Omega)$
C	$(\Omega, 2\Omega), (-\Omega, -2\Omega)$
D	$(\Omega, 0), (-\Omega, 0)$

In Figure 9, we notice that peaks from quartets C and D are elongated in the second axis. This point is also understood in the above argument, from which we have Table 4.

TABLE 4: Peak Widths for Quartets

quartet	width of peaks for (ω_1, ω_2)
A, B	(γ, γ)
C, D	$(\gamma, 2\gamma)$

A2. Double Modes (Weak Damping). Figure 10 shows signals from the system with two weak damping modes ($\Omega_1 = 1$, $\gamma_1 = 0.1\Omega_1$, $\Omega_2 = 0.5$, $\gamma_2 = 0.1\Omega_2$, in arbitrary units, with the assumption that $x_1^{(s)}$, $x_2^{(ss')}$ and, $M_s\zeta_s$ are all independent of mode indices (s and s')). Signals from each Liouville-space quartet are shown separately. We can interpret each signal in the following way.

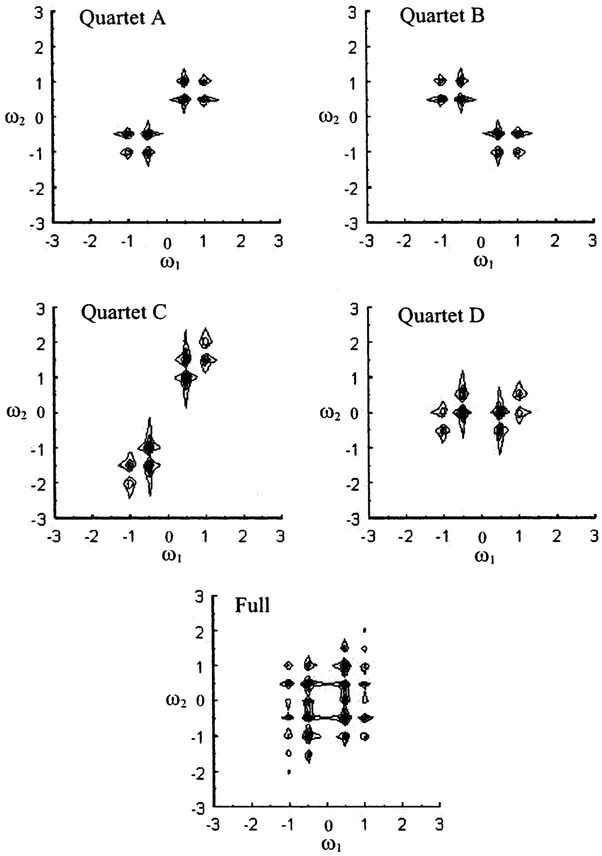

Figure 10. Contour plot of the signal from the system with two weakly damped modes.

Top-Left Plot of Figure 10. Two-mode quartet A2 in Figure 7 is associated with

$$\left\{\begin{array}{cccl} |1\rangle\langle 0| & \to & - & (\text{mode } s)\\ - & \to & |1\rangle\langle 0| & (\text{mode } s')\end{array}\right. \Rightarrow \begin{cases}(\Omega_{10}^{(s)}, \Omega_{10}^{(s')})\\(\Gamma_{10}^{(s)}, \Gamma_{10}^{(s')})\end{cases} \tag{74}$$

and its complex conjugate; this quartet produces the four cross peaks at $(\omega_1, \omega_2) = \pm(\Omega_1, \Omega_2), \pm(\Omega_2, \Omega_1)$. The remaining four diagonal peaks at $(\omega_1, \omega_2) = \pm(\Omega_1, \Omega_1)$ and $\pm(\Omega_2, \Omega_2)$ originate from single-mode quartets A2 and A1 in Figure 6, which corresponds to the process

$$\left\{\begin{array}{cccl} |1\rangle\langle 0| & \to & |1\rangle\langle 0| & (\text{mode } s)\\ - & \to & - & (\text{mode } s')\end{array}\right. \tag{75}$$

and its conjugate. The widths in the ω_1 and ω_2 directions for the peak at $(\omega_1, \omega_2) = \pm(\Omega_s, \Omega_{s'})$ are $\Gamma_{10}^{(s)}$ and $\Gamma_{10}^{(s')}$, respectively. In the fully corrected BO model, they are $\gamma_s/2$ and $\gamma_{s'}/2$, respectively. Although there exists the effect of interference, the relative width is consistent with this indication. For example, this is the reason that the peaks at (1, 0.5) and (0.5, 1) are elongated in the ω_1 and ω_2 axes, respectively. In summary, in the fully corrected BO model, the positions of peaks and two component of width are given by

$$\text{A2/A1(single mode): } \begin{cases}\pm(\Omega_1, \Omega_1) \text{ with } (\gamma_1/2, \gamma_1/2)\\ \pm(\Omega_2, \Omega_2) \text{ with } (\gamma_2/2, \gamma_2/2)\end{cases} \tag{76}$$

$$\text{A2 (two mode): } \begin{cases}\pm(\Omega_1, \Omega_2) \text{ with } (\gamma_1/2, \gamma_2/2)\\ \pm(\Omega_2, \Omega_1) \text{ with } (\gamma_2/2, \gamma_1/2)\end{cases} \tag{77}$$

Top-Right Plot of Figure 10. Single-mode quartet B in Figure 6 and two-mode quartet B in Figure 7 are associated with

$$\left\{\begin{array}{llll} |1\rangle\langle 0| & \rightarrow & |1\rangle\langle 2| & (\text{mode } s) \\ - & \rightarrow & - & (\text{mode } s') \end{array}\right. \Longrightarrow \left\{\begin{array}{l} (\Omega^{(s)}_{10}, \Omega^{(s')}_{12}) \\ (\Gamma^{(s)}_{10}, \Gamma^{(s')}_{12}) \end{array}\right. \tag{78}$$

$$\left\{\begin{array}{llll} |1\rangle\langle 0| & \rightarrow & - & (\text{mode } s) \\ - & \rightarrow & |0\rangle\langle 1| & (\text{mode } s') \end{array}\right. \Longrightarrow \left\{\begin{array}{l} (\Omega^{(s)}_{10}, \Omega^{(s')}_{01}) \\ (\Gamma^{(s)}_{10}, \Gamma^{(s')}_{01}) \end{array}\right. \tag{79}$$

The single-mode quartet produces the four diagonal peaks in the top-right plot whereas the two-mode quartet produces the four cross peaks. The widths in the two directions for the diagonal peaks are given by $(\Gamma^{(s)}_{10}, \Gamma^{(s')}_{12})$ whereas those for the cross peaks are given by $(\Gamma^{(s)}_{10}, \Gamma^{(s')}_{12})$. In summary, we have

$$\text{B (single mode):} \left\{\begin{array}{l} \pm(\Omega_1, -\Omega_1) \text{ with } (\gamma_1/2, \gamma_1/2) \\ \pm(\Omega_2, -\Omega_2) \text{ with } (\gamma_2/2, \gamma_2/2) \end{array}\right. \tag{80}$$

$$\text{B (two mode):} \left\{\begin{array}{l} \pm(\Omega_1, -\Omega_2) \text{ with } (\gamma_1/2, \gamma_2/2) \\ \pm(\Omega_2, -\Omega_1) \text{ with } (\gamma_2/2, \gamma_1/2) \end{array}\right. \tag{81}$$

Middle-Left Plot of Figure 10. Single-mode quartet C in Figure 6 and two-mode quartet C in 7 are associated with

$$\left\{\begin{array}{llll} |1\rangle\langle 0| & \rightarrow & |2\rangle\langle 0| & (\text{mode } s) \\ - & \rightarrow & - & (\text{mode } s') \end{array}\right. \Longrightarrow \left\{\begin{array}{l} (\Omega^{(s)}_{10}, \Omega^{(s')}_{20}) \\ (\Gamma^{(s)}_{10}, \Gamma^{(s')}_{20}) \end{array}\right. \tag{82}$$

$$\left\{\begin{array}{llll} |1\rangle\langle 0| & \rightarrow & |1\rangle\langle 0| & (\text{mode } s) \\ - & \rightarrow & |1\,\langle 0| & (\text{mode } s') \end{array}\right. \Longrightarrow \left\{\begin{array}{l} (\Omega^{(s)}_{10}, \Omega^{(s)}_{10} + \Omega^{(s')}_{10}) \\ (\Gamma^{(s)}_{10}, \Gamma^{(s)}_{10} + \Gamma^{(s')}_{01}) \end{array}\right. \tag{83}$$

The single-mode quartet produces the four overtone peaks in the middle-left plot whereas the two-mode quartet produces the four cross peaks. In summary, we have

$$\text{C (single mode):} \left\{\begin{array}{l} \pm(\Omega_1\ 2\Omega_1) \text{ with } (\gamma_1/2, \gamma_1) \\ \pm(\Omega_2, 2\Omega_2) \text{ with } (\gamma_2/2, \gamma_2) \end{array}\right. \tag{84}$$

$$\text{C (two mode):} \left\{\begin{array}{l} \pm(\Omega_1, \Omega_1 + \Omega_2) \text{ with } (\gamma_1/2, (\gamma_1 + \gamma_2)/2) \\ \pm(\Omega_2, \Omega_2 + \Omega_1) \text{ with } (\gamma_2/2, (\gamma_1 + \gamma_2)/2) \end{array}\right. \tag{85}$$

Middle-Right Plot of Figure 10. Single-mode quartets D1 and D2 in Figure 6 are associated with

$$\left\{\begin{array}{llll} |1\rangle\langle 0| & \rightarrow & |0\rangle\langle 0| & (\text{mode } s) \\ - & \rightarrow & - & (\text{mode } s') \end{array}\right. \Longrightarrow \left\{\begin{array}{l} (\Omega^{(s)}_{10}, \Omega^{(s)}_{00}) \\ (\Gamma^{(s)}_{10}, \Gamma^{(s)}_{00}) \end{array}\right. \tag{86}$$

$$\left\{\begin{array}{llll} |1\rangle\langle 0|\rangle & \rightarrow & |1\rangle\langle 1| & (\text{mode } s) \\ - & \rightarrow & - & (\text{mode } s') \end{array}\right. \Longrightarrow \left\{\begin{array}{l} (\Omega^{(s)}_{10}, \Omega^{(s)}_{11}) \\ (\Gamma^{(s)}_{10}, \Gamma^{(s)}_{11}) \end{array}\right. \tag{87}$$

whereas two-mode quartet D2 in 7 is associated with

$$\left\{\begin{array}{llll} |1\rangle\langle 0| & \rightarrow & |1\rangle\langle 0| & (\text{mode } s) \\ - & \rightarrow & |0\rangle\langle 1| & (\text{mode } s') \end{array}\right. \Longrightarrow \left\{\begin{array}{l} (\Omega^{(s)}_{10}, \Omega^{(s)}_{10} - \Omega^{(s')}_{10}) \\ (\Gamma^{(s)}_{10}, \Gamma^{(s)}_{10} + \Gamma^{(s')}_{01}) \end{array}\right. \tag{88}$$

The single-mode quartet produces the four axial peaks in the middle-right plot whereas the two-mode quartet the four cross-peaks. In summary, we have

$$\text{D1/D2 (single mode):} \left\{\begin{array}{l} \pm(\Omega_1, 0) \text{ with } (\gamma_1/2, \gamma_1) \\ \pm(\Omega_2, 0) \text{ with } (\gamma_2/2, \gamma_2) \end{array}\right. \tag{89}$$

$$\text{D2 (two mode):} \left\{\begin{array}{l} \pm(\Omega_1, \Omega_1 - \Omega_2) \text{ with } (\gamma_1/2, (\gamma_1 + \gamma_2)/2) \\ \pm(\Omega_2, \Omega_2 - \Omega_1) \text{ with } (\gamma_2/2, (\gamma_1 + \gamma_2)/2) \end{array}\right. \tag{90}$$

Note here that in the fully corrected BO model we have $\Gamma^{(s)}_{00} = \Gamma^{(s)}_{11}$ so that the widths from single-mode quartets D1 and D2 are the same as in the above.

The total signal is displayed at the bottom of the Figure; *we can assign each peak with distinct Liouville-space paths or energy-level diagrams* (as in Figure 8).

B. Time Domain. Figure 11 shows the contour plots of peaks from each quartet for a single over-damped mode system ($\Omega = 2\pi$, $\gamma = 6\pi$). Each quartet contributes to the total signal in a rather different way. This suggests the possibility of Liouville-space-path selective spectroscopy.

XI. Signals from the Brownian Oscillator Model and the Redfield-Type Model

In Figure 12, we compare results from two models: (1) the Brownian oscillator (BO) model (the system−bath interaction is fully taken into account), where we use eq 36 and (2) the Redfield-type model (RT), where we use eq 37 with the replacement $\zeta_s \rightarrow \Omega_s$ (no frequency shift).

Top. The right plot from the RT model has extra peaks on the left (BO) at $(\omega_1, \omega_2) = \pm(2, 1)$. They originate from the survival of quartets I and II in Figure 6.

Middle. On the left plot (BO), there exist extra peaks at $(\omega_1, \omega_2) = \pm(1, -1)$. These correspond to single-mode quartet B in Figure 6. For this process, the relaxation constants associated with the ω_2 axis, Γ_{12}, in BO and RT are given by γ and 3γ, respectively; the relaxation in RT is much faster, which explains the disappearance of the peaks. The peaks at $(\omega_1, \omega_2) = \pm(0.5, -0.5)$ survive because these peaks come not only from the single-mode process B but in this case the peaks from quartets I and II also overlap with those from other quartets.

Bottom. On the right plot (RT), there exist extra peaks at $(\omega_1, \omega_2) = \pm(0.3, 0.6)$. They corresponds to the survival of I and II in Figure 6.

In summary, the detailed situation depends on the parameters. However, they have one thing in common: the difference between the models is manifested in the existence or absence of certain peaks. The numerical results given above are all in the weak damping regime ($\gamma \approx 0.1\Omega$). The weak effect nonetheless affects the existence and absence of certain peaks. This is because the damping constants have a direct bearing on the cancellation mechanism of certain processes. Note that the situation is completely different for *weak* potential anharmonicity or nonlinear polarizability. Such weak effects, on the contrary, do not involve delicate cancellation mechanisms. (Although the difference between the left and right plots in Figure 12 seems to be small on a whole, if we concentrate on peaks that appear in one model but disappear in another model, we notice that the peak intensity can be fairly strong compared with that of other dominant (stable) peaks even though the damping constant used there is weak. The difference between models thus can be fairly strong, although they might be obscured by other effects.)

If the system exhibits a nonweak anharmonicity of potential or nonlinear system−bath coupling, as mentioned before, then there may be peaks at similar positions, as predicted by the

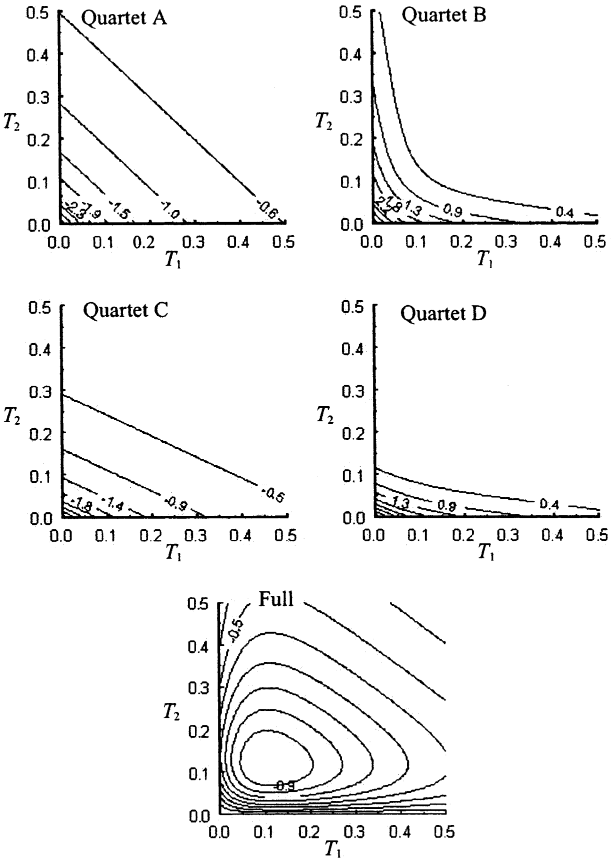

Figure 11. Contour plot of the signal from the system with a single over-damped mode.

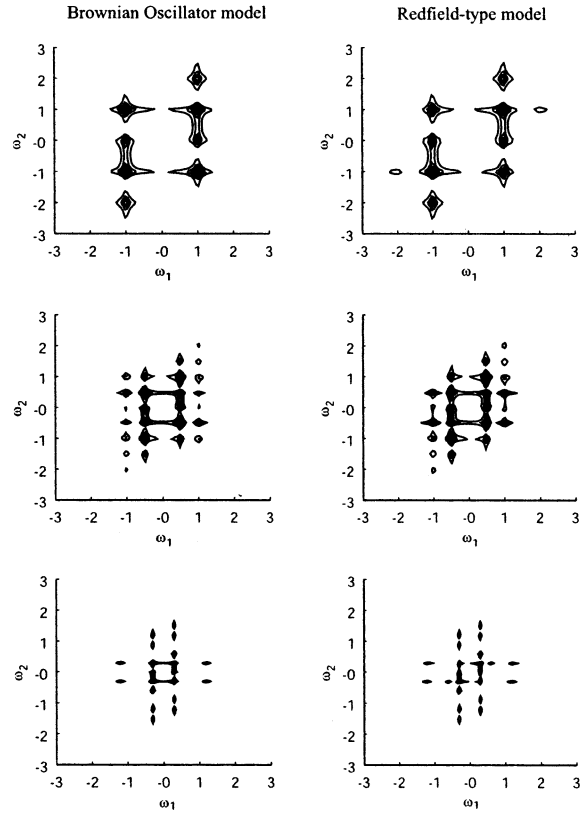

Figure 12. 2D signal from the two models. Top: single mode, $\Omega_1 = 1$. Middle: two modes, $\Omega_1 = 1$, $\Omega_2 = 0.5$. Bottom: two modes, $\Omega_1 = 1.2$, $\Omega_2 = 0.3$. Depending on the parameters, the difference between the models is manifested in the existence or nonexistence of diagonal peaks.

Redfield-type model. Such a mechanism, however, affects not only the existence of these peaks but also the entire profile of the signals, which involves different Liouville paths. The careful study of the signal in the frequency domain shall be the critical test of the Redfield-type model.

XII. Concluding Remarks

We stated an interpretation of the energy-level diagrams in the Liouville space and summarized the relationships between several diagrammatic representations. We emphasized that all of the diagrammatic representations reduce to unique interpretations in Liouville space, by which we can write down analytical expression by a Feynman rule.

We have given examples in which each Liouville process makes a distinctly unique contribution to a 2D signal; the selective detection of quantum processes by ultrafast spectroscopy might be possible. (For example, if we use multicolor 2D spectroscopy to study high-frequency vibrational modes, then we might utilize the phase-matching condition.[41]) By a suitably prepared spectroscopic configuration, we might be able to concentrate on a certain quantum process that allows a simpler analysis and a more quantitative understanding. Such Liouville-space-path selective spectroscopy might be promising. This situation reminds us of an analogy (although the principles might be quite different) in which the photon echo can be distinguished from the pump−probe via a phase-matching condition; we could differentiate spectroscopic methods by the peaks they produce.

An Energy-level diagram is useful in interpreting the physical process but only after confirming that the diagram makes a nonzero contribution possibly by another method. For example, in the (fully corrected) Brownian oscillator model, we can assume that the initial state of the diagram is the ground state because we know that other initial states result in the same contribution from a separate calculation. Another example is the cancellation of I by II in Figure 6.

In this respect, the diagram in the field-theoretical context, for example, which was introduced in ref 6, has some advantages. The number of diagrams to be considered is considerably smaller, and an analytical expression is obtained much more simply; in the case of $R^{(2)}(T_1, T_2)$, we have to consider only two diagrams, each being given by the product of two certain propagators, because the cancellation is always automatically taken into account in this method and, in addition, quartets are summed from the beginning in a simpler form. However, this conceals physical processes in the Liouville space.

If the initial temperature of the system is higher than the excitation energy of the vibrational levels (as in the case of low-frequency modes) or if the nonlinearity of the dipole or Raman transitions is important,[6,13,15] then we have to include a number of Liouville paths, especially in higher-order spectroscopy; the assignment of the peaks to some Liouville paths becomes nontrivial.

As for models of relaxation, we have considered only the system that is bilinearly coupled to the bath. We constructed the Feynman rule by starting from the rule in the case without damping, and then we replaced the propagator so that it causes damping with an appropriate choice of the relaxation parameters Γ_{mn}. One may think that the set $\{\Gamma_{mn}\}$ is an arbitrary set of parameters to fit experimental data; in the case of vibrational spectroscopy, however, Γ_{mn}'s have to satisfy certain universal relationships; for example, they have to satisfy the detailed balance condition. In addition, the validity of the rotating wave approximation (RWA) and the Markovian approximation associated with the second-order perturbation of the system−bath interaction might become questionable in vibrational spectroscopy; the characterization of the relaxation processes by simple rate constants such as T_1 and T_2 might not work. Note here that, although there are some restrictions, one can calculate the signals without using such approximations for the Brownian model, even in the anharmonic case.[6,31,35,52] To verify the consistency of the theory, it is important to compare the results from energy-level models and the Brownian motion model, where the latter is based upon a microscopic picture for damping.

To demonstrate how approximations for relaxation processes can change the results, we presented the 2D signals from the Redfield-type model and (full-order) Brownian oscillator model, and we observed that two models give peaks at different positions, even for weak damping. This, in turn, suggests a high sensitivity of 2D spectroscopy to damping models. This situation is in good contrast with cross peaks associated with mode coupling of an anharmonic or nonlinear origin, where they have to be fairly strong to be observable when diagonal peaks due to other effects are present. On the contrary, the cancellation mechanism is subtle, and thus, a weak damping effect can cause a drastic difference.

One of the purposes of our paper is to bridge the two complementary approaches of the coordinate-based and energy-level-based models. The results give us a useful interpretation of the coordinate-based model in the energy-level language. We should note, however, that this interpretation becomes precise only in the weak damping limit. Nonetheless, we believe that it is useful to have a common interpretation for the two approaches in certain situations.

Acknowledgment. We appreciate T. Kato and Y. Suzuki for critically reading our manuscript prior to submission. K.O. expresses his gratitude to P.-G. de Gennes and members of his group at Collège de France, including David Quéré, for warm hospitality during his third stay in Paris, which is financially supported by Collège de France. Y.T. is grateful for financial support from a Grant-in-Aid for Scientific Research (B) (12440171) from the Japan Society for the Promotion of Science and the Morino Science Foundation. This work is also supported by an internal grant from Ochanomizu University.

Appendix: Expression for $R^{(2)}(\omega_1, \omega_2)$

$2R^{(2)}(\omega_1, \omega_2)$ is given by eq (47) with each term expressed as

$$\mathrm{I}_s = \frac{f_{ss}}{(\omega_1 - z_{20}^{(s)})(\omega_2 - z_{10}^{(s)})} + \frac{f_{ss}}{(\omega_1 + [z_{20}^{(s)}]^*)(\omega_2 + [z_{10}^{(s)}]^*)} \tag{A.1}$$

$$\mathrm{II}_s = -\frac{f_{ss}}{(\omega_1 - z_{20}^{(s)})(\omega_2 - z_{21}^{(s)})} - \frac{f_{ss}}{(\omega_1 + [z_{20}^{(s)}]^*)(\omega_2 + [z_{21}^{(s)}]^*)} \tag{A.2}$$

$$(\mathrm{A2})_{ss'} = \frac{f_{ss'}}{(\omega_1 - z_{10}^{(s)})(\omega_2 - z_{10}^{(s')})} + \frac{f_{ss'}}{(\omega_1 + [z_{10}^{(s)}]^*)(\omega_2 + [z_{10}^{(s)}]^*)} \tag{A.3}$$

$$\mathrm{B}_s = -\frac{f_{ss}}{(\omega_1 - z_{10}^{(s)})(\omega_2 - z_{12}^{(s)})} - \frac{f_{ss}}{(\omega_1 + [z_{10}^{(s)}]^*)(\omega_2 + [z_{12}^{(s)}]^*)} \tag{A.4}$$

$$\mathrm{B}_{ss'} = -\frac{f_{ss'}}{(\omega_1 - z_{10}^{(s)})(\omega_2 - z_{01}^{(s')})} - \frac{f_{ss'}}{(\omega_1 + [z_{10}^{(s)}]^*)(\omega_2 + [z_{01}^{(s)}]^*)} \tag{A.5}$$

$$\mathrm{C}_s = \frac{f_{ss}}{(\omega_1 - z_{10}^{(s)})(\omega_2 - z_{20}^{(s)})} + \frac{f_{ss}}{(\omega_1 + [z_{10}^{(s)}]^*)\,(\omega_2 + [z_{20}^{(s)}]^*)} \tag{A.6}$$

$$\mathrm{C}_{ss'} = \frac{f_{ss'}}{(\omega_1 - z_{10}^{(s)})(\omega_2 - (z_{10}^{(s)} + z_{10}^{(s')}))} + \frac{f_{ss'}}{(\omega_1 + [z_{10}^{(s)}]^*)(\omega_2 + [z_{10}^{(s)} + z_{10}^{(s)\prime}]^*)} \tag{A.7}$$

$$(\mathrm{D2})_{ss'} = -\frac{f_{ss'}}{(\omega_1 - z_{10}^{(s)})(\omega_2 - (z_{10}^{(s)} + z_{01}^{(s')}))} - \frac{f_{ss'}}{(\omega_1 + [z_{10}^{(s)}]^*)(\omega_2 + [z_{10}^{(s)} + z_{01}^{(s')}]^*)} \tag{A.8}$$

$$2\mathrm{D1}_s = \frac{f_{ss}}{(\omega_1 - z_{10}^{(s)})(\omega_2 - z_{00}^{(s)})} + \frac{f_{ss}}{(\omega_1 + [z_{10}^{(s)}]^*)(\omega_2 + [z_{00}^{(s)}]^*)} \tag{A.9}$$

$$\frac{2}{3}\,\mathrm{D2}_s = -\frac{2f_{ss}}{(\omega_1 - z_{10}^{(s)})(\omega_2 - z_{11}^{(s)})} - \frac{2f_{ss}}{(\omega_1 + [z_{10}^{(s)}]^*)(\omega_2 + [z_{11}^{(s)}]^*)} \tag{A.10}$$

where

$$z_{nm}^{(s)} = \zeta_{nm}^{(s)} - i\Gamma_{nm}^{(s)}$$

Note Added after ASAP Posting. This article was posted ASAP on 5/20/2003. Changes were made to eqs 47, 55, and 58. The correct version was posted on 6/26/2003.

References and Notes

(1) Mukamel, S. *Principles of Nonlinear Optical Spectroscopy*; Oxford University Press: New York, 1995.

(2) Tanimura, Y.; Mukamel, S. *J. Chem. Phys.* **1993**, *99*, 9496.

(3) Tominaga, K.; Yoshihara, K. *Phys. Rev. Lett.* **1995**, *74*, 3061.

(4) Steffen, T.; Duppen, K. *Phys. Rev. Lett.* **1996**, *76*, 1224.

(5) Tokmakoff, A.; Fleming, G. R. *J. Chem. Phys.* **1997**, *106*, 2569.

(6) Okumura, K.; Tanimura, Y. *J. Chem. Phys.* **1997**, *107*, 2267. Okumura, K.; Tanimura, Y. *J. Chem. Phys.* **1997**, *106*, 1687.

(7) Saito, S.; Ohmine, I. *J. Chem. Phys.* **1998**, *108*, 240.

(8) Cho, M.; Okumura, K.; Tanimura, Y. *J. Chem. Phys.* **1998**, *108*, 1326.

(9) Kirkwood, J. C.; Albrecht, A. C.; Ulness, D. J. *J. Chem. Phys.* **1999**, *111*, 253. Kirkwood, J. C.; Albrecht, A. C.; Ulness, D. J.; Stimson, M. J. *J. Chem. Phys.* **1999**, *111*, 272.

(10) Jansen, T. I. C.; Snijders, J. G.; Duppen, K. *J. Chem. Phys.* **2001**, *114*, 10910.

(11) Golonzka, O.; Demirdoven, N.; Khalil, M.; Tokmakoff, A. *J. Chem. Phys.* **2000**, *113*, 9893.

(12) Kubarych, K. J.; Milne, C. J.; Lin, S.; Astinov, V.; Miller, R. J. D. *J. Chem. Phys.* **2002**, *116*, 2016. Kubarych, K. J.; Milne, C. J.; Lin, S.; Miller, R. J. D. *Appl. Phys. B* **2002**, *74*, S107.

(13) Saito, S.; Ohmine, I. *Phys. Rev. Lett.* **2002**, *88*, 207401.

(14) Blank, D. A.; Kaufman, L. J.; Fleming, G. R. *J. Chem. Phys.* **2000**, *113*, 77.

(15) Kaufman, L. J.; Heo, J.; Ziegler, L. D.; Fleming, G. R. *Phys. Rev. Lett.* **2002**, *88*, 207402.

(16) Denny, R. A.; Reichman, D. R. *Phys. Rev. E* **2001**, *63*, R065101. Denny, R. A.; Reichman, D. R. *J. Chem. Phys.* **2002**, *116*, 1987.

(17) Cao, J.; Wu, J.; Yang, S. *J. Chem. Phys.* **2002**, *116*, 3760.

(18) Ma, A.; Stratt, R. M. *Phys. Rev. Lett.* **2000**, *85*, 1004. Ma, A.; Stratt, R. M. *J. Chem. Phys.* **2002**, *116*, 4962. Ma, A.; Stratt, R. M. *J. Chem. Phys.* **2002**, *116*, 4972.

(19) Keyes, T.; Fourkas, J. T. *J. Chem. Phys.* **2000**, *112*, 287. Kim, J.; Keyes, T. *Phys. Rev. E* **2002**, *65*, 061102.

(20) Hamm, P.; Lim, M.; Hochstrasser, R. M. *J. Phys. Chem. B* **1998**, *102*, 6123.

(21) Woutersen, S.; Hamm, P. *J. Chem. Phys.* **2001**, *115*, 7737.

(22) Golonzka, O.; Kahlil, M.; Demirdoven, N.; Tokmakoff, A. *J. Chem. Phys.* **2001**, *115*, 10814.

(23) Sung, J.; Silbey, R. J.; Cho, M. *J. Chem. Phys.* **2001**, *115*, 1422.

(24) Mukamel, S. *Annu. Rev. Phys. Chem.* **2000**, *51*, 691.

(25) Fourkas, J. T. *Adv. Chem. Phys.* **2001**, *117*, 235.

(26) Cho, M. *PhysChemComm* **2002**, *7*, 1.

(27) Ge, N. H.; Hochstrasser, R. M. *PhysChemComm* **2002**, *3*, 1.

(28) Wright, J. C. *Int. Rev. Phys. Chem.* **2002**, *21*, 185.

(29) Oxtoby, D. W. *Adv. Chem. Phys.* **1979**, *40*, 1. Oxtoby, D. W. *Adv. Chem. Phys.* **1981**, *47*, 487.

(30) Redfield, A. G. *Adv. Magn. Reson.* **1965**, *1*, 1.

(31) Okumura, K.; Tanimura, Y. *Phys. Rev. E* **1996**, *53*, 214. Okumura, K.; Tanimura, Y. *J. Chem. Phys.* **1996**, *105*, 7294.

(32) Okumura, K.; Tanimura, Y. *Chem. Phys. Lett.* **1997**, *277*, 159.

(33) Okumura, K.; Tanimura, Y. *Chem. Phys. Lett.* **1997**, *278*, 175.

(34) Suzuki, Y.; Tanimura, Y. *J. Chem. Phys.* **2001**, *115*, 2267.

(35) Suzuki, Y.; Tanimura, Y. *Chem. Phys. Lett*. **2002**, *358*, 51.

(36) Lee, D.; Albrecht, A. C. *Adv. Infrared Raman Spectrosc.* **1985**, *12*, 179.

(37) Steffen, T.; Fourkas, J. T.; Duppen, K. *J. Chem. Phys.* **1996**, *105*, 7364.

(38) Murry, R. L.; Fourkas, J. T. *J. Chem. Phys.* **1997**, *107*, 9726.

(39) Tominaga, T.; Maekawa, H. *Bull. Chem. Soc. Jpn.* **2001**, *74*, 279.

(40) Golonzka, O.; Tokmakoff, A. *J. Chem. Phys.* **2001**, *115*, 297.

(41) Kato, K.; Tanimura, Y. *Chem. Phys. Lett*. **2001**, *341*, 329.

(42) Park K.; Cho, M. *J. Chem. Phys.* **1998**, *109*, 10559.

(43) Cho, M. In *Advances in Multi-Photon Processes and Spectroscopy*; Lin, S. H., Villaeys, A. A., Fujimura, Y., Eds.; World Scientific: Singapore, 1999; Vol. 12, p 229.

(44) Zhao, W.; Wright, J. C. *Phys. Rev. Lett.* **1999**, *83*, 1950. Zhao, W.; Wright, J. C. *J. Am. Chem. Soc.* **1999**, *121*, 10994. Zhao, W.; Wright, J. C. *Phys. Rev. Lett.* **2000**, *84*, 1411.

(45) Cho, M.; Hess, C.; Bonn, M. *Phys. Rev. B* **2002**, *65*, 205423.

(46) Grabert, H.; Shramm, P.; Ingold, G.-L. *Phys. Rep.* **1988**, *168*, 115.

(47) Weiss, U. *Quantum Dissipative Systems*, 2nd ed.; World Scientific: Singapore, 1999.

(48) Fourkas, J. T.; Kawashima, H.; Nelson, K. A. *J. Chem. Phys.* **1995**, *103*, 4393.

(49) Sung, J.; Cho, M. *J. Chem. Phys.* **2000**, *113*, 7072.

(50) Kato, K.; Tanimura, Y. *J. Chem. Phys.* **2002**, *117*, 6221.

(51) Tanimura, Y.; Wolynes, P. G. *Phys. Rev. A* **1991**, *43*, 4131. Tanimura, Y.; Wolynes, P. G. *J. Chem. Phys.* **1992**, *96*, 8485.

(52) Tanimura, Y. *Chem. Phys*. **1988**, *233*, 217.

(53) Steffen, T.; Tanimura, Y. *J. Phys. Soc. Jpn.* **2000**, *69*, 3115.

(54) Tanimura, Y.; Steffen, T. *J. Phys. Soc. Jpn.* **2000**, *69*, 4095.

(55) Kato, K.; Tanimura, Y. *J. Chem. Phys.*, submitted for publication.

(56) Tokmakoff, A.; Lang, M. J.; Larsen, D. S.; Fleming, G. R.; Chernyak V.; Mukamel, S. *Phys. Rev. Lett.* **1997**, *79*, 2702.